Journal of Statistical Physics (2026) 193:124
https://doi.org/10.1007/s10955-026-03651-w

Statistical Modeling of Bifractal Statistics with a Superposition of Characteristic Functionals

Gabriel B. Apolinário[1] · **Michael Wilczek**[1]

Received: 18 December 2025 / Accepted: 11 June 2026 / Published online: 17 September 2026
© The Author(s) 2026

Abstract
Turbulent fields display intermittent and skewed observables as some of their main features, but translating them to multipoint statistics remains a challenge. This work constructs a pseudo-characteristic functional inspired by the statistics of the one-dimensional Burgers velocity field. The functional is chosen as an ensemble of nearly Gaussian basis functionals with fluctuating typical scales, and the distribution of the fluctuating scale is such that one-point velocity statistics are Gaussian, while increments and gradients show bifractal statistics. This behavior can be obtained from the asymptotic properties of the base and scale distributions. Skewness is added with a functional Taylor expansion and truncation of a characteristic functional, producing statistics compatible with the Burgers analog of the 4/5 law.

Keywords Multifractals · Bifractal statistics · Mixture distribution · Characteristic functionals

1 Introduction

Turbulent velocity fields are naturally random objects. This approach, pioneered in the 1930s [1], translates the effects of chaos and the many degrees of freedom in a flow, to the question of determining field statistics. The main statistical features observed in numerical simulations and experiments are non-Gaussian and heavy-tailed fluctuations of small-scale observables [2–4]. Furthermore, these distributions are not self-similar, as shown by scale-dependent quantities such as velocity increments or wavelet coefficients [5]. This loss of self-similarity is called intermittency [6].

Previous studies have constructed intermittent distributions of some multi-scale observables. For instance, Gaussian mixture models have been proposed for Lagrangian acceleration [7, 8] and velocity increment distributions [9, 10]. However, a description of the entire Eulerian velocity field statistics in this mixture approach is still lacking. In this direction,

Communicated by Massimo Vergassola.

✉ Gabriel B. Apolinário
gapolinario@uni-bayreuth.de

Michael Wilczek
michael.wilczek@uni-bayreuth.de

[1] Theoretical Physics I, University of Bayreuth, Universitätsstr. 30, 95447 Bayreuth, Germany

multifractal phenomenology in Navier-Stokes turbulence establishes a connection between the universal behavior of different observables, and has provided successful predictions. As an example, the universal exponents of the following observables have been derived from the Eulerian increment statistics: Velocity gradients [11, 12], Lagrangian increments [13], and products of Eulerian increments and gradients [14, 15]. This phenomenology was used in [9] to create a consistent model of increments and gradients, even though it does not present a functional probability density.

This paper addresses the construction of probability densities for one-dimensional fields as a statistical ensemble of simpler fields: That is, the characteristic functional $\Phi[\widetilde{\alpha}]$ of a field is decomposed into base functionals $\Phi_s[\widetilde{\alpha}]$ with a parameter s, which is distributed according to the PDF f. The base functional is one with a simple analytical expression: For that we have chosen the Gaussian functional and a perturbative expansion of the Gaussian similar to a Gram-Charlier series. The mixture functional is then written as $\Phi[\widetilde{\alpha}] = \int ds f(s)\Phi_s[\widetilde{\alpha}]$. Such an approach bridges the gap between low-dimensional mixtures of the last paragraph and high-dimensional Gaussian mixtures, which have found applications in a diversity of fields [16–19] . We focus on infinite-dimensional statistics, i.e., the statistics of intermittent fields, as addressed in a recent study [20]. This previous study observed that one can build intermittent distributions by choosing the typical scale of the Gaussian correlation function as a so-called ensemble decomposition variable, whose value varies across the ensemble.

We introduce two new elements to the ensemble formulation of [20]: Intermittency exponents and skewness. The ensemble decomposition has been explored for symmetric or positive variables in Lagrangian acceleration [8] and curvature statistics [21], respectively. However, a hallmark of turbulent statistics is the asymmetry in the PDFs of small-scale observables. This asymmetry, related to skewness, is added to the ensemble through an approximate characteristic functional, built as a truncation of a general characteristic functional, in the spirit of the Gram-Charlier A series. Expansions of this type have been used to describe one-dimensional distributions of nearly Gaussian observables [22–24] and are adapted to the functional context in this work.

Regarding the exponents, we specify a choice of ensemble distribution $f(s)$ that yields bifractal statistics, as shown by structure function and velocity gradient moment exponents. Our study of bifractal behavior is motivated by Burgers turbulence, where the exponents can be obtained analytically [6, 12, 25, 26]. Moreover, bifractal statistics has been observed in other recent studies in statistical fluid dynamics. We mention, for instance, Lagrangian pair dispersion in shock-dominated turbulence [27], circulation in Navier-Stokes [28], circulation in quantum turbulence [29], and viscous fingering [30].

The paper is organized as follows: In Sect. 2, we discuss the phenomenology of Burgers turbulence as inspiration for the bifractal statistics. The Gaussian ensemble decomposition approach is reviewed in Sect. 3. Sect. 4 discusses how to obtain bifractal statistics with an ensemble. A dissipative scale and gradient statistics are discussed in Sect. 5. Skewness is added in Sect. 6. These results are extended to nonsmooth subensembles in Sect. 7. Conclusions and future perspectives are presented in Sect. 8.

2 Burgers Turbulence

The stochastic Burgers equation is a classic one-dimensional PDE similar to the Navier-Stokes equations in many aspects. It defines the evolution of a velocity field u with the

equation

$$\partial_t u + u\partial_x u = \nu \partial_x^2 u + f, \tag{1}$$

where ν is viscosity and a stochastic forcing f acts on the large spatial scales L. The nonlinear term produces a direct cascade, carrying energy from the large to the small scales. This equation is fully compressible, hence shocks are formed, which are eventually smoothened out at the smallest scales by the viscous term. The balance between self-advection and dissipation defines a dissipative scale (η_K) which is proportional to the viscosity (contrary to Navier-Stokes, where it is proportional to $\nu^{3/4}$). The behavior of the dissipative scale with ν can be observed in a typical shock solution, such as the Khokhlov sawtooth [31, 32],

$$u(x,t) = \frac{1}{t}\left[x - L\tanh\frac{Lx}{2\nu t}\right], \tag{2}$$

whose Fourier modes decay exponentially if $k \gg 1/\nu$. At intermediate scales ℓ, with $\eta_K \ll \ell \ll L$, an inertial range with bifractal statistics is observed: Consider, for instance, the velocity increment at scale ℓ, defined as

$$\delta_\ell u(x) = u(x+\ell) - u(x). \tag{3}$$

The increments are statistically homogeneous (that is, any statistic depends only on ℓ and not on x), and their moments behave as [25, 33]

$$\langle |\delta_\ell u|^p \rangle \underset{\ell\to 0}{\propto} \ell^{\min(1,p)}. \tag{4}$$

In this equation, we use the proportionality symbol in an asymptotic sense, meaning

$$f(x) \underset{x\to L}{\propto} g(x), \text{ iff } \lim_{x\to L}\frac{f(x)}{g(x)} = C \text{ for some positive constant } C. \tag{5}$$

For details and a proof of Eq. (4), the reader is referred to Boritchev and Kuksin [26]. This picture of Burgers turbulence is valid in the limit of large Reynolds numbers, defined as $\mathrm{Re} = UL/\nu$, where U is a typical large-scale velocity, such as the mean intensity of the shocks.

As observed by Aurell et al. [25], the scaling of Eq. (4) corresponds, in the multifractal formalism, to a field with only two Hölder exponents. An exponent $H = 1$ is observed in smooth regions of the velocity field, as ascending ramps, while $H = 0$ represents sudden negative shocks, which are present in the limit of vanishing viscosity (equivalently infinite Reynolds number). The shocks and ramps produce statistics heavily skewed towards negative velocity gradients and velocity increments: The positive gradients show sub-Gaussian fluctuations [34], while the negative gradients are heavy-tailed [35]. Skewness is also manifest in the following exact result, equivalent to the 4/5-law in Navier-Stokes turbulence [36]:

$$\langle (\delta_\ell u)^3 \rangle \underset{\ell\to 0}{\sim} -12\varepsilon\ell, \tag{6}$$

where ε is a positive constant, the mean energy dissipation, $\varepsilon = \nu\langle (u_x)^2\rangle$. For further studies on intermittency and the statistics of stochastic Burgers turbulence, see for instance [15, 26, 37–39].

3 Ensembles of Fields

To describe the statistics of velocity fields that capture some of the features of Burgers turbulence we use the characteristic functional. Consider a scalar field u in one-dimensional

space, $x \in \mathbb{R}$: Its characteristic functional is given by

$$\Phi[\widetilde{\alpha}] = \left\langle \exp\left\{ i \int_{\mathbb{R}} \mathrm{d}x\, \widetilde{\alpha}(x) u(x) \right\} \right\rangle, \tag{7}$$

where the angle brackets denote an average over independent realizations of the field u. Arbitrary multi-point statistical observables of the velocity are obtained through an appropriate choice of the function $\widetilde{\alpha}$. For instance, the characteristic *function* of the field at a point x is

$$\Phi_{u(x)}(\alpha) \coloneqq \Phi[\widetilde{\alpha} = \alpha\delta(\cdot - x)] = \left\langle e^{i\alpha u(x)} \right\rangle. \tag{8}$$

Square brackets are used to indicate functional parameters and parentheses for scalar parameters. The characteristic function for the velocity gradient at x is

$$\Phi_{u_x(x)}(\alpha) \coloneqq \Phi[\widetilde{\alpha} = -\alpha\delta'(\cdot - x)] = \left\langle e^{i\alpha u_x(x)} \right\rangle, \tag{9}$$

where δ' indicates the derivative of a Dirac delta function. For velocity increments at scale ℓ and at a point x the characteristic function is

$$\Phi_{\delta_\ell u(x)}(\alpha) \coloneqq \Phi\left[\widetilde{\alpha} = \alpha\big(\delta(\cdot - x - \ell) - \delta(\cdot - x)\big)\right] = \left\langle e^{i\alpha\delta_\ell u(x)} \right\rangle. \tag{10}$$

From now on, the point x is omitted from the notation since we consider only statistically homogeneous fields.

An important property of Eq. (7) is that a convex linear combination of characteristic functionals produces another characteristic functional,

$$\Phi[\widetilde{\alpha}] = \int \mathrm{d}s\, f(s) \Phi_s[\widetilde{\alpha}], \tag{11}$$

where s is a possibly multi-dimensional random parameter indexing the subensemble functionals (Φ_s) and distributed according to the PDF $f(s)$. This construction is called a mixture distribution [16], which was explored in the context of continuous fields to build intermittent characteristic functionals with Gaussian subensembles [20]. A Gaussian characteristic functional, after explicit integration of Eq. (7), is given by

$$\Phi^G[\widetilde{\alpha}; s] = \exp\left\{ i \int_{\mathbb{R}} \mathrm{d}x\, \mu(x; s)\widetilde{\alpha}(x) - \frac{1}{2} \int_{\mathbb{R}^2} \mathrm{d}x\mathrm{d}x'\, \widetilde{\alpha}(x) C_2(x, x'; s) \widetilde{\alpha}(x') \right\}, \tag{12}$$

where we have added a clear dependence on the ensemble parameter s. As a next step, we choose $\mu(x; s) = 0$, $C_2(x, x'; s) = C_2(x - x'; s)$ and identify $s > 0$ with the typical length of the correlation function C_2, meaning that

$$C_2(x; s) = \sigma^2 \left(1 - \frac{x^2}{2s^2} + O(x^3) \right), \tag{13}$$

with $\sigma > 0$. As a consequence the ensemble field is of zero mean, statistically homogeneous and intermittent. This expansion also provides a physical interpretation of the scale s as equivalent to the Taylor scale in turbulence.

Regarding intermittency, observe that, as σ is not a function of s, the single-point PDF of the velocity field is always Gaussian:

$$\Phi_u(\alpha) = \int \mathrm{d}s\, f(s) \exp\left\{ -\frac{1}{2}\alpha^2 C_2(0; s) \right\} = e^{-\frac{1}{2}\alpha^2\sigma^2}. \tag{14}$$

On the other hand, the velocity gradient statistics are heavy-tailed: The velocity gradient PDF is

$$\Phi_{u_x}(\alpha) = \int \mathrm{d}s\, f(s)\, \exp\left\{-\frac{1}{2}\alpha^2 |C_2''(0;s)|\right\} = \int \mathrm{d}s\, f(s)\, e^{-\frac{\alpha^2\sigma^2}{2s^2}}, \tag{15}$$

where the derivatives are taken with respect to the spatial argument. With Jensen's inequality one observes that the kurtosis (normalized fourth-order moment) of this distribution is

$$\kappa = \frac{\langle (u_x)^4 \rangle}{\langle (u_x)^2 \rangle^2} = \frac{\int \mathrm{d}s\, f(s)(3\sigma^4/s^4)}{\left(\int \mathrm{d}s\, f(s)(\sigma^2/s^2)\right)^2} \geq 3. \tag{16}$$

These observations are independent on the choice of the ensemble distribution f.

The statistics of increments at scale ℓ, therefore, interpolate between a Gaussian (at large scales) and a heavy-tailed PDF (at small scales). This dependence of the kurtosis on scale is a defining characteristic of intermittency [6] and, besides the argument above, is observed in the examples and figures in [20].

4 Bifractal Ensemble

In this section we describe how we obtain bifractal exponents with an ensemble of Gaussian fields [20] and an explicit choice of the distribution f. The symbol $\propto$ represents proportionality in an asymptotic limit, that is,

$$f(x) \underset{x\to L}{\propto} g(x) \text{ iff there is } C \in (0,\infty) \text{ s.t. } \lim_{x\to L} \frac{f(x)}{g(x)} = C. \tag{17}$$

Consider an ensemble of Gaussian fields as described by Eqs. (11) to (13). Let $m > 0$ and $\eta > 0$ be parameters for a family of random distributions, and choose a PDF whose asymptotic behavior is

$$f_m(s;\eta) \underset{s\to 0^+}{\propto} (s/\eta)^{m-1}. \tag{18}$$

The ensemble field produced in this manner displays bifractal statistics. More specifically, the one-point velocity is Gaussian, as seen in Eq. (14), and its structure functions satisfy

$$\langle (\delta_\ell u)^n \rangle_m \underset{\ell\to 0^+}{\propto} (\ell/\eta)^{\min(m,n)}, \tag{19}$$

for $m \neq n$, even n. Furthermore, if $m = n$,

$$\langle (\delta_\ell u)^n \rangle_m \underset{\ell\to 0^+}{\propto} (\ell/\eta)^n \log(\eta/\ell). \tag{20}$$

As we show in the following, the statistics are a consequence of the asymptotic scaling of the ensemble distribution and on the fact that the subensemble fields are smooth. We assume f_m to be the PDF of a rescaled Beta$(m, 1)$ distribution:

$$f_m(s;\eta) = m(s/\eta)^{m-1}, \text{ if } 0 \leq s \leq \eta. \tag{21}$$

Define the function

$$S_2(\ell; s) \coloneqq 2C_2(0;s) - 2C_2(\ell;s), \tag{22}$$

in terms of which the increment characteristic function is written as

$$\Phi_{\delta_\ell u}(\alpha) = \int \mathrm{d}s\, f_m(s;\eta)\, \exp\left\{-\tfrac{1}{2} S_2(\ell;s)\alpha^2\right\}. \tag{23}$$

Since the subensembles are Gaussian distributions, the even increment moments are

$$\langle(\delta_\ell u)^{2p}\rangle_m = (2p-1)!! \int \mathrm{d}s\, f_m(s;\eta) S_2^p(\ell;s). \tag{24}$$

In the inertial range, $\ell \ll L$, $S_2(\ell;s) \propto (\ell/s)^2$ and this integral is essentially $\int_0^\eta \mathrm{d}s\,(s/\eta)^{m-1}(\ell/s)^{2p}$, which is proportional to ℓ^{2p} if $2p < m$. If $2p > m$, however, this simple integral diverges and it becomes important to consider the behavior of S_2 at large arguments. A simplified representation of a structure function is:

$$S_2(\ell;s) = \begin{cases} 2(\ell/s)^2, & \text{if } \ell/s < 1 \\ 2, & \text{if } \ell/s > 1. \end{cases} \tag{25}$$

Given that $\eta > \ell$, this integral produces two terms, respectively proportional to ℓ^n and ℓ^m. Additionally, the log term in Eq. (20) is obtained from Eq. (25).

A more detailed proof is given in Sect. A.2, where the assumption of the Beta distribution is relaxed. We remark that Eqs. (19) and (20) are also valid for the absolute value structure functions, $\langle|\delta_\ell u|^n\rangle_m$, with $n > 0$: Since the absolute value subensemble moments are also proportional to $(\ell/s)^n$, the previous proof carries over identically. Regarding the f_m distribution, there are other well known probability distributions besides the Beta$(m,1)$ with the same asymptotic behavior (Eq. (18)). For instance, the Erlang and Nakagami distributions, both with semi-infinite support. The parameterizations we use are $f_m^E(s;\eta) = e^{-ms/\eta} s^{-1+m}(m/\eta)^m/\Gamma(m)$ for the Erlang PDF and $f_m^N(s;\eta) = 2^{1-m/2} e^{-m(s/\eta)^2/2} s^{-1+m}(m/\eta^2)^{m/2}/\Gamma(m/2)$ for the Nakagami PDF. After this reparametrization, the typical scale of these distributions is η. Because of this freedom in choosing f_m, the integration range in s is usually not indicated.

We can also compute the large fluctuation tails of the velocity gradient PDF. The characteristic function for u_x is

$$\Phi_{u_x}(\alpha) = \int \mathrm{d}s\, f_m(s;\eta)\, e^{-\frac{1}{2}\alpha^2 G_2(s)}, \tag{26}$$

with the definition

$$G_2(s) \coloneqq -C_2''(0,s) = (\sigma/s)^2. \tag{27}$$

Choosing f_m as the Beta distribution and with a change of variables $z = s\xi$, one shows that the velocity gradient PDF $\mathcal{P}_{u_x}$ displays power-law behavior:

$$\mathcal{P}_{u_x}(\xi) = \int_0^\eta \mathrm{d}s\, f_m(s;\eta)\, \frac{s}{\sqrt{2\pi}\sigma} e^{-\frac{1}{2}(s\xi/\sigma)^2} \underset{\xi\to\infty}{\propto} \xi^{-m-1}. \tag{28}$$

From this power-law behavior we conclude that the n-th statistical moment of the velocity gradient distribution is undefined if $n \geq m$. A more detailed proof of Eq. (28) can be found in Sect. A.4: It relies only on asymptotic estimates, meaning that it is valid for any distribution satisfying Eq. (18).

We remark that the decay of the velocity gradient PDFs in Burgers turbulence is not of the form in Eq. (28). To begin with, Burgers velocity gradients are skewed, an element which is added to the ensemble formulation in Sect. 6. As observed in [40, 41], the negative tail of the velocity gradient PDF in the inviscid case is proportional to $|u_x|^{-7/2}$. This discrepancy is discussed in Sect. 6, where skewness is added.

A comparison of Eq. (28) against numerical simulations is seen in Fig. 1. The Gaussian subensemble moments were computed analytically, and integrated numerically against the f_m distribution. In (a), we see standardized increment PDFs for different scales ℓ. It transitions

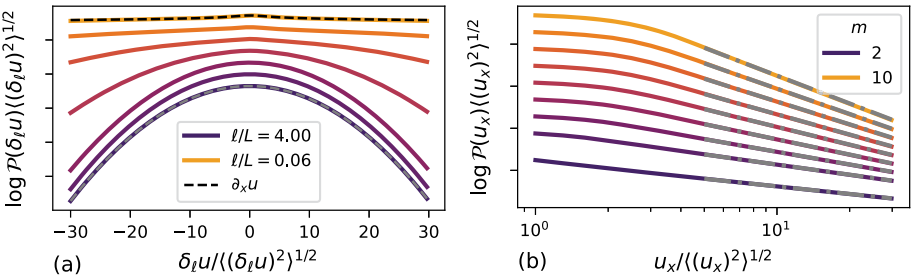

Fig. 1 (a) Standardized velocity increment PDFs at different scales ℓ for $m = 5$ and s distributed as a Beta$(m, 1)$ random variable. At large scales they approach a Gaussian PDF, indicated with a gray dashed line. At small scales, they show larger deviations. In black, the velocity gradient PDF, Eq. (28), is shown. PDFs have been arbitrarily shifted upwards for ease of visualization (for this reason marks on the vertical axis are omitted). (b) Large deviation tails of the standardized velocity gradient PDFs (colors) compared to power-law fits (gray) for different values of m. The exponent of the power-law decay is fixed at $-m - 1$, following Eq. (28). The variance of the gradient diverges for $m = 1$ and is not shown

from Gaussian (gray dashed curve), at $\ell \approx L$, to a power-law decay at $\ell \ll L$. In black, the velocity gradient PDF is plotted. It was computed in the same way, with numerical integration of the analytical subensemble PDF. In this figure, $m = 5$ and s follows a Beta$(m, 1)$ distribution, with similar results observed for other values of m and other distributions. A good agreement is observed in the Gaussian and the power-law limits. In (b), the tails of velocity gradient PDFs for different values of m are compared against the respective power-law fits, in gray. A fit of the form $a \times u_x^{-m-1}$ was chosen, with the exponent fixed according to Eq. (28). For $m = 1$, the velocity gradient variance diverges and we are not able to normalize it, hence it is not shown in the plot. In all cases, the standard error is of less than 1%, relative to the best fit for a.

We conclude this section with an outline for a sampling algorithm: For each of them, one samples a value of s from the f_m distribution, followed by generating a Gaussian field with correlation function $C_2(x, s)$ by a standard method (a spectral method, for instance). For each Gaussian field, s is fixed, while for an ensemble of such fields, the fluctuations of s are responsible for intermittency.

5 Viscous Regime

As observed in Sect. 4, velocity gradient moments of order $n > m$ in the ensemble diverge (Eq. (28)). In turbulent one-dimensional flows, however, this behavior is regularized at any finite Reynolds number by the presence of a dissipation scale $\eta_K \propto \nu \propto \mathrm{Re}^{-1}$. We reproduce this effect in the ensemble by modifying the argument of C_2 as $x^2 \to x^2 + \nu^2$. With this change, the increments remain bifractal in the inertial range ($\nu \ll \ell \ll L$), while in the dissipative range ($\ell \ll \nu$) increments and gradients scale as

$$\langle(\delta_\ell u)^p\rangle_m \underset{\ell\to 0^+}{\propto} \ell^p \mathrm{Re}^{\max(0,p-m)} \quad \text{and} \quad \langle(u_x)^p\rangle_m \underset{\mathrm{Re}\to\infty}{\propto} \mathrm{Re}^{\max(0,p-m)}. \tag{29}$$

With the choice $m = 1$, Eq. (29) reproduces the dissipation-range statistics of Burgers turbulence, first described in [11, 12]. After this regularization, the velocity PDF is no longer exactly Gaussian, but deviations are of order $O(\nu^2)$ and vanish in the limit of infinite Reynolds

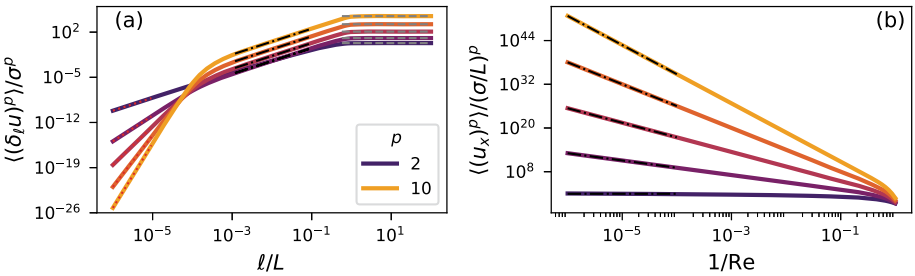

Fig. 2 p-order structure functions at different values of p. The subsensembles are Gaussian and zero-mean, therefore all the odd moments are zero. In (a), we see ensemble structure functions, with the ensemble distribution Beta($m = 2, 1$). Red dotted lines indicate power-law fits with fixed exponent, $a \times \ell^p$, corresponding to the viscous range. In the dissipative range, the exponents of the fits are set to $\min(m, p)$, and shown in black dashed-dotted lines. In the large-scale range, Gaussian behavior is recovered, which is indicated by analytical results in gray dashed lines. In (b), scaling of the velocity gradient moments with viscosity is shown, together with power-law fits with exponent $\mathrm{Re}^{\max(0,p-m)}$

number. A proof of the gradient scaling in Eq. (29) can be found in Sect. A.3, it relies on the asymptotic scaling of C_2 and f_m, but not on their exact forms.

For the numerical simulations, we choose the correlation function

$$C_2(x; s, \nu) = \sigma^2 e^{-(x^2+\nu^2)/2s^2}, \tag{30}$$

and ensemble structure functions are computed with Eq. (24). Results for the ensemble and subensemble structure functions can be seen in Fig. 2 with the following parameters: The ensemble distribution is Beta(m, 1) with $m = 2$. The velocity variance is $\sigma = 1$, and viscosity is $\nu = 10^{-4}$.

In Fig. 2(a), ensemble structure functions of different orders p are shown, overlayed by asymptotic results and power-law fits. In this plot, the structure function exponent ζ_p, defined by

$$\langle(\delta_\ell u)^p\rangle_m \underset{\ell\to 0^+}{\propto} \ell^{\zeta_p}, \tag{31}$$

was measured in two different ways. We show in red dotted lines a power-law fit of the form $a \times \ell^p$, with the exponent fixed according to the analytical prediction for smooth behavior. This fit provides visual confirmation of the exponents. Another fit with free exponent ($a \times \ell^b$) was done to confirm this visual inspection, and the results of the free exponent fits are shown in Fig. 3 In the inertial range, black dashed-dotted lines indicate power-laws with exponents $\zeta_p = \min(m, p)$. Still in Fig. 2(a), at large separation, the Gaussian limit is recovered, and the moments of a Gaussian distribution with mean zero and variance σ^2 are displayed with gray dashed lines.

In Fig. 2(b), the scaling of the velocity gradient moments with viscosity is shown, computed with

$$\langle(u_x)^p\rangle = (p-1)!! \int \mathrm{d}s\, f_m(s; \eta) G_2^{p/2}(s, \nu). \tag{32}$$

The analytical velocity gradient exponent $\xi_p = \max(0, p - m)$, defined by $\langle(u_x)^p\rangle_m \underset{\mathrm{Re}\to\infty}{\propto} \mathrm{Re}^{\xi_p}$, is shown in the black dashed-dotted lines.

The exponents ζ_p and ξ_p, measured numerically, are compared against the analytical prediction of bifractal behavior in Fig. 3. In (a), the structure function exponents for different values of m (in colors) are compared to bifractal exponents ($\zeta_p = \min(m, p)$, in black

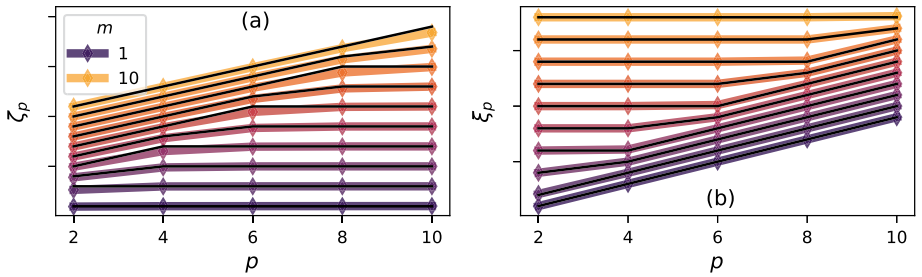

Fig. 3 Scaling exponents of the increment and gradient moments, computed with numerical fits of the form $a \times \ell^b$ ($a \times \mathrm{Re}^b$) for the increments (gradients), respectively. The horizontal axis indicates the order of the statistical moments and different colors represent the m parameters for the ensemble distribution, Eq. (18). The values of the exponents have been shifted vertically to allow for easier visualization, therefore the label values on the vertical axis are omitted. In (a), scaling exponents of the structure functions in the inertial range are observed. Black lines show the analytical bifractal result, $\zeta_p = \min(m, p)$. In (b), the exponents corresponding to the scaling of velocity gradient moments are shown and compared with the bifractal $\xi_p = \max(0, p - m)$ (black lines)

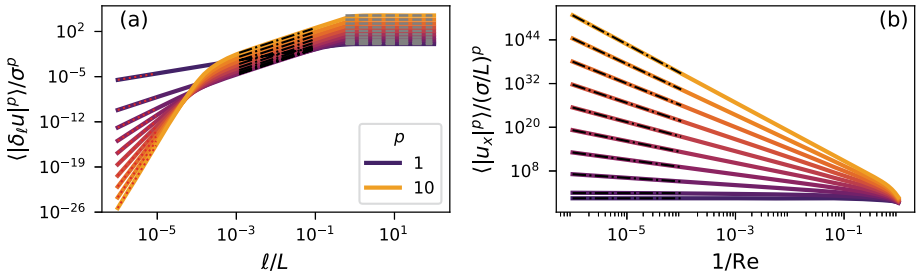

Fig. 4 p-order absolute value moments of increments and gradients with ensemble parameter $m = 2$. In (a), structure functions are shown and in (b) the velocity gradient scaling with Reynolds. The black dashed-dotted lines indicate power-laws obtained with a fit, and their extent represents the fitting range

lines). The same analysis was done in the dissipation range to confirm the linear and smooth exponents, $\zeta_p = p$ (data not shown). The analytical curves and numerical fits show good agreement, with a slight deviation from the analytical curve at the transition points $m = p$. We attribute this to the log-corrections in the exponent, as observed in Eq. (20). Fig. 3(b) shows the gradient exponents compared to the bifractal result, $\xi_p = \max(0, p - m)$.

Since the subensembles are Gaussian, its odd moments are null. However, we can compute absolute value moments of increment and gradient moments, which are shown in Fig. 4. They were computed with

$$\langle|\delta_\ell u|^p\rangle = \frac{2^{p/2}}{\sqrt{\pi}}\Gamma\left(\frac{1+p}{2}\right)\int \mathrm{d}s\; f_m(s;\eta)S_2^{p/2}(\ell;s,\nu) \text{ and} \tag{33a}$$

$$\langle|u_x|^p\rangle = \frac{2^{p/2}}{\sqrt{\pi}}\Gamma\left(\frac{1+p}{2}\right)\int \mathrm{d}s\; f_m(s;\eta)G_2^{p/2}(s,\nu), \tag{33b}$$

where Γ is the Gamma function. Compared to Fig. 2, only ensemble increments and gradients are shown in Fig. 4, together with fixed-exponent power-law fits for the different scaling ranges. The exponents remain the same and can be seen in Fig. 5, compared to the bifractal predictions. Exponents of fractional order are shown in Fig. 6, in increments of 0.2 (the individual markers are omitted for clarity). This is an important confirmation that this ensemble

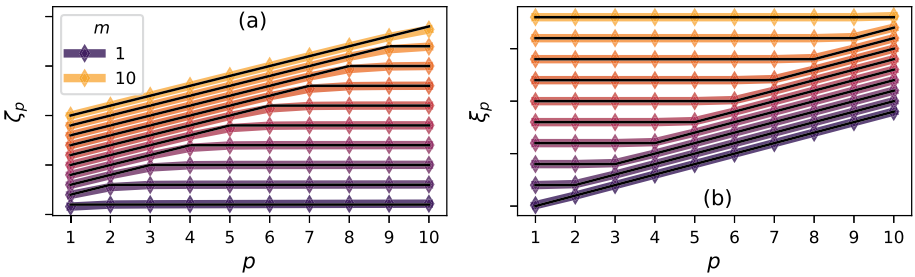

Fig. 5 Bifractal exponents of the absolute value moments of increments and gradients. As in Fig. 3, (a) shows the structure function exponents and (b) the gradient exponents. Since they are computed for absolute value moments, odd values of p can now be included. Black lines also indicate the bifractal results, $\zeta_p = \min(m,\, p)$ and $\xi_p = \max(0,\, p - n)$

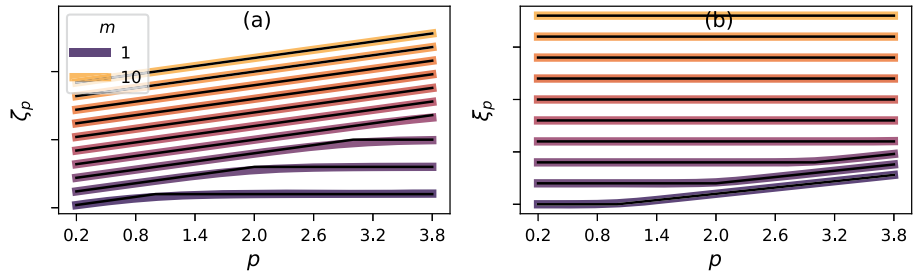

Fig. 6 Bifractal exponents of absolute value moments of increments and gradients. Fractional values of the moment order were chosen to highlight the bifractal transition illustrated by Burgers turbulence, i.e. $\zeta_p = p$ for $p < 1$ and $\zeta_p = 1$ for $p \geq 1$, corresponding to the line with $m = 1$. Individual points are not shown, as in Fig. 5, so as to keep the plot more accesible

statistics is bifractal, when compared to the Burgers literature, where the linear behavior $\zeta_p = p$ is observed for $p < 1$.

6 Skewness with a Truncated Characteristic Functional

Skewness is a base element of turbulent flows, as made evident by the 4/5-law (or 12-law in Burgers turbulence, Eq. (6)). To introduce it in the ensemble formulation, we consider a general characteristic functional defined by a functional Taylor expansion:

$$\Phi[\widetilde{\alpha}] = \exp\left\{\sum_{n=2}^{\infty} \frac{i^n}{n!} \int_{\mathbb{R}^n} \left(\prod_{j=1}^{n} \mathrm{d}x_j \widetilde{\alpha}(x_j)\right) C_n(\delta\mathbf{x})\right\}, \tag{34}$$

where the functions C_n only depend on $n-1$ arguments (due to homogeneity), denoted by the vector $\delta\mathbf{x} = (x_1 - x_2, \ldots, x_1 - x_n)$. We have also chosen a zero-mean field by starting the sum at $n = 2$. It is known that any finite truncation of Eq. (34) at order larger than 2 cannot produce a true characteristic functional [42, Thm. 7.3.3 (Marcinkiewicz)]. However, if the C_3 and higher-order terms are small, we have an approximation to weakly non-Gaussian fields similar to the Gram-Charlier A series, an approximation that has found many applications in the one-dimensional setting (see [22–24, 43] for a small sample). In the rest of this paper, we use the lowest-order truncation of Eq. (34) which produces skewed subensembles:

$$\Phi[\widetilde{\alpha}; s] = \exp\Big\{ -\frac{1}{2}\int_{\mathbb{R}^2} \mathrm{d}x_1\mathrm{d}x_2\, \widetilde{\alpha}(x_1)\widetilde{\alpha}(x_2)C_2(x_1 - x_2; s) - \frac{i}{6}\int_{\mathbb{R}^3} \mathrm{d}x_1\mathrm{d}x_2\mathrm{d}x_3\, \widetilde{\alpha}(x_1)\widetilde{\alpha}(x_2)\widetilde{\alpha}(x_3)C_3(x_1 - x_2, x_1 - x_3; s)\Big\}. \tag{35}$$

In order for the one-point velocity distribution to be Gaussian (in the inviscid regime), we choose C_3 such that $C_3(0, 0; s) = 0$. For the numerical simulations,

$$C_3(x, y; s) = \mu^3 \frac{(x + y)}{s} e^{-(x^2+y^2)/2s^2}, \tag{36}$$

where μ is a real parameter that determines the skewness. The $(x+y)$ contribution is important to guarantee the skewness of increments and gradients do not vanish, in contrast to symmetric terms such as $\sqrt{x^2 + y^2}$.

From Eq. (35), the velocity-gradient one-point distribution, after the ensemble integration, is

$$\Phi_{u_x}(\alpha) = \int \mathrm{d}s\, f_m(s; \eta)\, e^{-\frac{1}{2}\alpha^2 G_2(s) - \frac{i}{6}\alpha^3 G_3(s)}, \tag{37}$$

with

$$G_3(s) \coloneqq C_3^{(2,1)}(0, 0; s) + C_3^{(1,2)}(0, 0; s), \tag{38}$$

where the derivatives are taken with respect to the spatial arguments, x and y. The increment distribution is

$$\Phi_{\delta_\ell u}(\alpha) = \int \mathrm{d}s\, f_m(s; \eta) \exp\left\{-\frac{1}{2}\alpha^2 S_2(\ell; s) - \frac{i}{6}\alpha^3 S_3(\ell; s)\right\}, \tag{39}$$

with S_3 defined as

$$S_3(\ell; s) \coloneqq C_3(\ell, \ell; s) + C_3(-\ell, 0; s) - C_3(0, \ell; s) + C_3(0, -\ell; s) - C_3(\ell, 0; s) - C_3(-\ell, -\ell; s). \tag{40}$$

The statistical moments of these two distributions can be written in terms of the *complete exponential Bell polynomials*, represented by B_n (see Comtet [44, p. 139, Thm. C]):

$$\langle (u_x)^p \rangle = (-i)^p \frac{\partial^p \Phi_{u_x}(\alpha)}{\partial \alpha^p}\bigg|_{\alpha=0} = \int \mathrm{d}s\, f_m(s; \eta)\, B_p(0, G_2(s), G_3(s), 0, \ldots, 0) \tag{41}$$

(equivalently for Eq. (39)). The B_p are functions of p arguments, whose generating function is the one-dimensional version of Eq. (34). For this reason the arguments of B_p in Eq. (41), for $p > 3$, are all zero. Furthermore, since $G_2(s) \propto 1/s^2$ and $G_3(s) \propto 1/s^3$, the polynomial in Eq. (41) is proportional to $1/s^p$, as can be seen from the definition of B_p. This is analogous to the behavior of the pth-order moments in the symmetric case, therefore the argument for bifractal behavior of Sect. A.3 extends to the skewed case for even and odd moments. It also extends to the increment moments, since $S_3(\ell; s) \propto (\ell/s)^3$, as assumed in Sect. A.2.

We can furthermore interpret the distributions given by Eqs. (37) and (39) as superpositions of Gaussian fields using the Airy formula, [45, 46]

$$\int_{\mathbb{R}} \mathrm{d}y\, \mathrm{Ai}(y) e^{iyw} = e^{-iw^3/3}, \tag{42}$$

with which we rewrite Eq. (37) as

$$\Phi_{u_x}(\alpha) = \int \mathrm{d}s\, f_m(s; \eta) \int_{\mathbb{R}} \mathrm{d}y\, \mathrm{Ai}(y) \exp\left\{i\alpha y \sqrt[3]{\tfrac{1}{2}G_3(s)} - \frac{1}{2}\alpha^2 G_2(s)\right\}. \tag{43}$$

The Airy function plays the role of an ensemble distribution, especially if one notices that $\int_{\mathbb{R}} \mathrm{Ai}(y)\mathrm{d}y = 1$, even though it is not a non-negative function. Eqs. (37), (41) and (42), together with the statistical properties of Gaussian distributions, can be used to compute exact statistical moments of the increment and velocity gradient ensemble distributions. Furthermore, one can also compute moments of $|\delta_\ell u|$ and $|u_x|$ as an integration over s of the corresponding known results for Gaussian distributions. These can be used to show that the subensemble moments also behave like smooth functions, with $|\delta_\ell u|^p \propto (\ell/s)^p$ and $|u_x|^p \propto s^{-p}$.

What is more, with Eq. (43), we can show that the velocity gradient PDF has power-law tails with exponent $-m-1$, as in the symmetric case (Eq. (28)). To show that, we use Eq. (3.10) of [47], to obtain the skewed velocity gradient PDF:

$$\mathcal{P}_{u_x}(\xi) = \int \mathrm{d}s\, f_m(s;\eta) \int_{\mathbb{R}} \mathrm{d}y\, \mathrm{Ai}(y) \exp\left\{-\frac{1}{2G_2(s)}\left(\xi - y\sqrt[3]{G_3(s)/2}\right)^2\right\} \tag{44a}$$

$$= \int \mathrm{d}s\, f_m(s;\eta) \frac{1}{\sqrt[3]{G_3(s)/2}} \exp\left\{\frac{G_2^3(s) + 3\xi G_2(s) G_3(s)}{3G_3^2(s)}\right\}$$

$$\times\, \mathrm{Ai}\left(\frac{\xi}{\sqrt[3]{G_3(s)/2}} + \frac{G_2^2(s)}{2^{2/3} G_3^{4/3}(s)}\right). \tag{44b}$$

If $\mu > 0$, the gradient skewness is negative, and the negative tail is $\mathcal{P}_{u_x}(\xi) \propto |\xi|^{-m-1}$, exactly as in the symmetric case (Eq. (28)). For large positive gradients, though, there are non-physical oscillations in the gradient PDF. However, if we concentrate only on the upper envelope of this PDF, the same power-law decay is observed. Details for this derivation can be found in Sect. A.5, while numerical results are shown in Fig. 7.

At this point, it is important to discuss the quantitative difference between the tails of the Burgers velocity gradients and those of Eq. (44b). The stochastic Burgers velocity gradient PDF is given by $|u_x|^{-7/2}$ for the inviscid negative tail [40, 41] and by a sub-Gaussian decay, $\exp\left(-u_x^3\right)$, for the positive tail [34, 48]. Eq. (44b), however, differs in two important aspects from this result: (a) Its large deviation decay is symmetric, in that its negative tail is $|u_x|^{-m-1}$ and the *envelope* of its positive tail is also $|u_x|^{-m-1}$. The positive tail shows slowly decaying non-physical fluctuations due to the Airy function, which do not change the exponent of the envelope. And (b) the numerical value of the exponents differ. By choosing $m = 1$, the increment and gradient exponents of the ensemble model match Eq. (4), but the gradient PDF decays as $-m - 1 = -2$.

The exponents produced in the ensemble are the same that would arise from a linear model conditioned on random fields [49–51], which reveals a possible connection between the current approach and random PDEs. Such linear models generate Gaussian statistics, and therefore produce gradient exponents similar to the mixture above, instead of those of Burgers dynamics. One can also consider the conditioning procedure as the result of a slowly evolving random field, producing a patchwork of random fields with different random parameters, as in [52]. The patchwork interpretation is possibly close to to the recent observation of [53], who identified monofractal and multifractal regions within a turbulent flow.

We have investigated different classes of mixing functions $f_m(s)$, beyond the power-law type, but they fail to satisfy all of the properties of the current model: Converging integrals for the velocity gradient tails, as well as in the two bifractal regimes ($p > m$ and $p < m$). This leads us to believe that changing the gradient exponent would require non-Gaussian subensembles (with power-law tails, for instance).

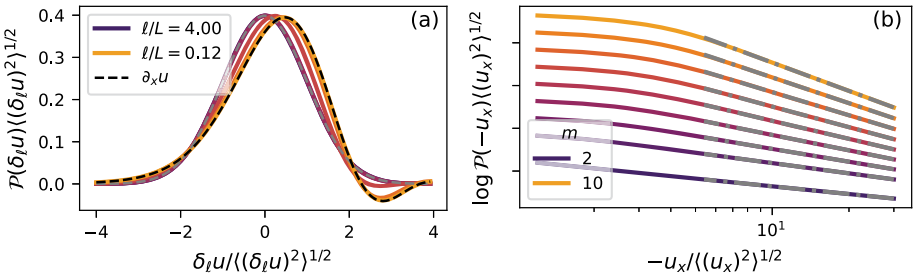

Fig. 7 (a) Standardized velocity increment PDFs at different separations for $m = 5$ and $\mu = 1$, in linear scale. At large scales they resemble a Gaussian PDF, indicated in a gray dashed line. At small scales, they show larger deviations, and negative oscillations stemming from the third-order truncation in Eq. (35). The velocity gradient PDF is shown in a black dashed line, which was integrated numerically as well. In (b), the negative tail of velocity gradient PDFs with different values of m are shown, together with numerical fits of power-law decay with exponent $-m - 1$ (gray dash-dotted). PDFs in (b) have been arbitrarily shifted upwards for ease of visualization

In Fig. 7(a), a linear plot of the standardized skewed PDF of velocity increments is shown, for $m = 5$ and $\mu = 1$ (all other parameters are the same as in Fig. 1). The numerical cost of evaluating the PDFs depends on the skewness, and different approaches were used at different scales. For intermediate ℓ, a numerical integration of

$$\mathcal{P}_{\delta_\ell u}(\delta u) = \int \mathrm{d}s\, f_m(s;\eta) \int_{\mathbb{R}} \mathrm{d}y\, \mathrm{Ai}(y) \exp\left\{-\frac{1}{2S_2(\ell;s)}\left(\delta u - y\sqrt[3]{S_3(\ell;s)/2}\right)^2\right\} \quad (45)$$

is done. Integration of the Airy function was performed with a routine for oscillating integrands [54], which explains the cost dependence: A higher skewness of the PDF decreases the separation between the zeros of the Airy function, therefore more terms are needed for the convergence of the corresponding integrals. For the gradient and small scales, skewness increases and Eq. (44b) can be used directly (together with its version for increments).

At large scales, the skewness vanishes and the increment PDF approaches a Gaussian, indicated in a gray dashed curve. At smaller scales, the PDF shows larger tails and negative oscillations. These negative oscillations are small, but show up in a log-linear plot as singularities, which render its visualization inadequate. In a linear plot, however, the transition from Gaussian to the negatively-skewed gradient PDF (in black dashed) is noticeable. In Fig. 7(b), the negative tail of the velocity gradient PDFs for different values of m are shown in log-log scale, together with power-law fits of the form $a \times u_x^{-m-1}$ in gray dash-dotted lines. In all cases, the standard error in the fits is of less than 1%.

Viscosity was also added to the skewed ensembles for the numerical evaluation of structure functions and gradient moments. It is included by modifying Eq. (36) to

$$C_3(x, y; s, \nu) = \mu^3 \frac{(x+y)}{s} e^{-(x^2+y^2+\nu^2)/2s^2}, \quad (46)$$

a form which preserves $C_3(0, 0; s, \nu) = 0$ and regularizes the gradients and increments at small scales. With this, we compute $\langle(\delta_\ell u)^p\rangle$, $\langle|\delta_\ell u|^p\rangle$, $\langle(u_x)^p\rangle$ and $\langle|u_x|^p\rangle$ with Eqs. (41) and (44a), and the properties of Gaussian distributions.

Fig. 8 shows ensemble structure functions (a) and gradients moments (b) with $m = 5$ and $\mu = 1$, for different integer values of the moment order p. The odd moments also follow bifractal scaling. In (a), at small scales, red dotted lines indicate smooth power-law fits ($a \times \ell^p$), and black dash-dotted lines represent bifractal power-law fits ($a \times \ell^{\min(m,p)}$). At

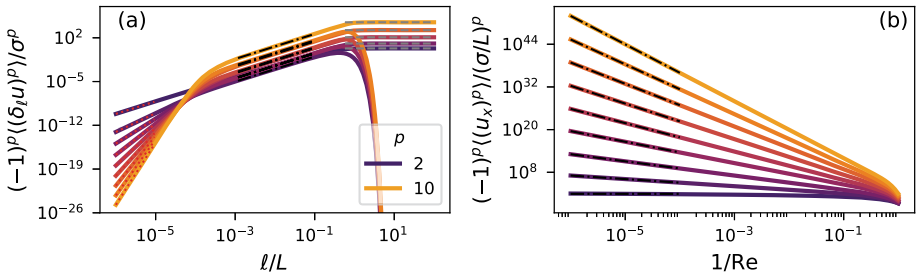

Fig. 8 (a) Structure functions of different order p as function of the separation ℓ. With the chosen parameters, $m = 5$ and $\mu = 1$, the odd-order moments are negative, but they are shown inverted. Red dotted lines indicate power-law fits with fixed exponent, $a \times \ell^p$, with the analytical exponents for smooth functions. Black dash-dotted lines represent bifractal power-law fits, $a \times \ell^{\min(m,p)}$. Gray dashed lines indicate the Gaussian limit at large scales, where all the odd order moments vanish. In (b), velocity gradient moments as functions of the Reynolds are shown, with the same parameters. The black dashed-dotted lines also indicate bifractal fits, with exponents $a \times \mathrm{Re}^{\max(0,p-m)}$

the large scales, the odd-order moments vanish and the even ones converge to the Gaussian limit (gray dashed). In Fig. 8(b), the scaling of the velocity gradient moments with Reynolds is indicated, and compared to the bifractal prediction (black dash-dotted lines).

Power-law fits with free exponents were computed for the increment and gradient moments, as well as for their absolute value counterparts. As expected, adding skewness doesn't change the values of the exponents observed in Fig. 5 (which are the exponents for absolute value increments and gradients). Therefore, the equivalent plot in the skewed case is not shown here.

7 Nonsmooth Subensembles

So far, we have considered Gaussian correlation functions C_2 and C_3 corresponding to smooth subensembles. However, this framework may be extended to rough subensembles, characterized by a Hölder exponent H, with $0 < H < 1$. One of the inspirations for this is the classic K41 theory of fluid turbulence [55], where structure function exponents are $\zeta_p = p/3$. Another source of bifractal behavior is the Wolf-Villain model [56, 57], which shows up in models with quenched disorder, such as viscous fingering [30]. In Bernard et al. [50], it was observed that height increments in a growth model are bifractal, with exponents

$$\langle |h(x,t) - h(0,t)|^q \rangle \propto x^{\zeta_q} L(t)^{q\zeta - \zeta_q}, \; x < L(t), \tag{47}$$

where the height of the surface is h, and the correlation length $L(t)$ increases with time. The exponents are $\zeta_q = \min(1, q\zeta)$ and $\zeta > 1/2$. In analogy with Eq. (19), $m = 1$ as in the Burgers case. This happens since the growing surfaces described by Eq. (47) are one-dimensional, forming shocks and nonsmooth ramps.

In this section we describe a system with scaling of the form

$$\langle (\delta_\ell u)^p \rangle \underset{\ell \to 0}{\propto} \ell^{\min(m, pH)}, \tag{48}$$

and equivalent results for the velocity gradient, which are compatible with the multifractal formalism [11, 12].

The Matérn function is a classic example of correlation function with rough increments, which inspired our choices in building nonsmooth subensembles. This function is used for instance in the generation of monofractal Gaussian fields [58–61], and is asymptotically proportional to $\ell^H K_H(\ell)$, where K_H is the modified Bessel function. In order to have Gaussian instead of simple exponential decay, we have chosen the correlation function

$$C_2^H(x;s) = \sigma^2 \frac{2^{1-H/2}}{\Gamma(H/2)} |x/s|^H K_{H/2}\left(x^2/s^2\right). \tag{49}$$

Notice that $C_2^H(0;s) = \sigma^2$ is independent on the ensemble parameter s.

For the skewed correlation function, we have chosen

$$C_3^H(x,y;s) = \mu^3 \frac{x+y}{s} \left(\frac{x^2+y^2}{s^2}\right)^{\frac{1}{2}(3H-1)} e^{-\frac{(x^2+y^2)}{2L^2}}, \text{ if } H \neq 1/3 \tag{50}$$

and

$$C_3^{1/3}(x,y;s) = \mu^3 \frac{x+y}{s} K_0\left(\sqrt{x^2+y^2}/s\right), \text{ for } H = 1/3, \tag{51}$$

where both equations satisfy $C_3^H(0,0;s) = 0$. Following the definitions for the corresponding S_2^H and S_3^H functions (Eqs. (22) and (40), respectively), we obtain the desired rough asymptotic behavior:

$$S_2^H(x;s) \underset{x\to 0}{\propto} (x/s)^{2H} \text{ and } S_3^H(x;s) \underset{x\to 0}{\propto} (x/s)^{3H}, \tag{52}$$

instead of the smooth scalings of Eq. (24). The above dual definition is a solution to the fact that, with Eq. (50), the increment $\lim_{H\to 1/3} S_3^H(x;s)$ is smooth (proportional to $(x/s)^3$), instead of the expected (x/s).

The scaling behavior of Eq. (52) can be easily estimated noticing that the K_α function, near the origin, behaves as $K_\alpha(x) \underset{x\to 0}{\propto} |x|^{\min(\alpha,-\alpha)}$. The constant term for S_2^H vanishes (see Eq. (22)), but the one for S_3 does not. Averaging over the ensemble distribution, Eq. (18), we obtain an equivalent bifractal behavior, this time with the smooth scaling exponent p replaced by pH:

$$\langle (\delta_\ell u)^p \rangle \underset{\ell\to 0^+}{\propto} \ell^{\min(m,pH)}. \tag{53}$$

For our numerical simulations of this system, we add a small viscous cutoff to C_2^H and $C_3^{1/3}$ with the replacement $x^2 \to x^2 + \nu^2$ ($x + y$ in Eq. (50) is unchanged, to preserve the symmetry of $C_3^{1/3}$). In this way, not only are the increment statistics bifractal, but the gradient moments are also finite and scale as

$$\langle (u_x)^p \rangle \underset{\mathrm{Re}\to\infty}{\propto} \mathrm{Re}^{\max(p(1-H),m-p)}, \tag{54}$$

in agreement with the multifractal phenomenology of [11, 12]. Below the viscous dissipation scale, both the ensemble and subensembles show smooth behavior.

The numerical results for the increment and gradient moments as functions of the scale and the Reynolds number, respectively, are seen in Fig. 9, with parameters $\sigma = 1$, $m = 2$, $\mu = 1.0$, and $H = 1/3$. In (a), the ensemble structure functions of order p are shown, while (b) shows ensemble gradient moments. A dissipative range is now observed in (a), and a power-law fit with fixed exponent $\zeta_p = p$ is overlayed (red dotted). In the inertial range, a similar power-law fit is done, with exponent $\min(m, pH)$ (bifractal). The same ensemble

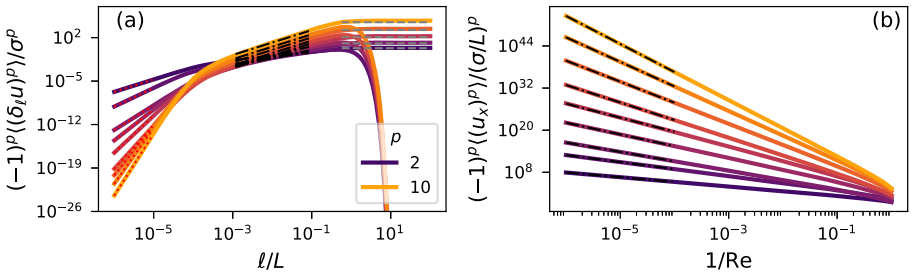

Fig. 9 Structure functions and gradient moments with a nonsmooth subensemble, as in Eq. (52). (a) shows the ensemble structure functions, and (b) the velocity gradient moments. In the dissipative range, seen in (a), power-law fits with exponent p are shown (red dotted). In the inertial range (black dash-dotted), the exponents are $\min(pH, m)$. For the gradient moments (b), a similar power-law fit was done with exponent $\max(p(H-1), p-m)$

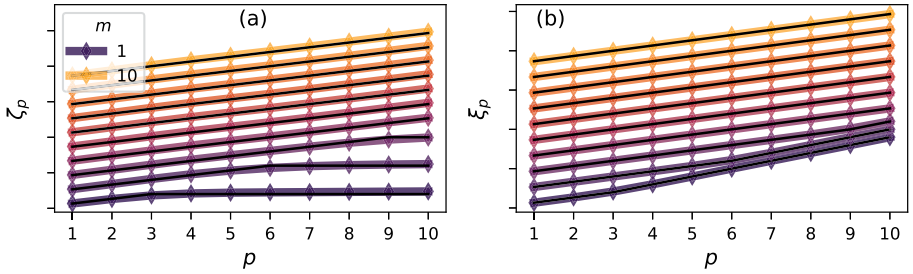

Fig. 10 Exponents of the absolute value structure functions and gradient moments with a nonsmooth subensemble, see Eq. (52). In (a), structure function exponents from power-law fits (colors) are shown together with the analytical results, $\zeta_p = \min(pH, m)$ (in black). In (b), the exponents of absolute velocity gradient moments are shown, compared to $\xi_p = \max(p(1-H), m-p)$

exponents were measured as well with power-law fits of the form $a \times \ell^b$ (resp. $a \times \mathrm{Re}^b$) and are shown in Fig. 10.

For the velocity gradient PDFs, observe that

$$G_2^H(s,\nu) = s^{-2}(\nu/s)^H \times \frac{2^{2-H/2}}{\Gamma(H/2)} K_{1-H/2}(\nu^2/s^2) \underset{\nu\to 0^+}{\propto} s^{-2H}\nu^{-2+2H}. \tag{55}$$

Integrating against the Beta function (as a model for f_m), and with the change of variables $u = \xi z^H$, we obtain

$$\mathcal{P}_{u_x}(\xi) = m\int_0^\eta \mathrm{d}s\,(s/\eta)^{m-1}\frac{1}{\sqrt{2\pi G_2^H(s,\nu)}}\exp\left[-\frac{\xi^2}{2G_2^H(s,\nu)}\right] \underset{\xi\to\infty}{\propto} \xi^{-m/H-1}. \tag{56}$$

This is numerically verified in the no-skewness case in Fig. 11. In (a), the standardized increment PDFs in log-linear scale are shown for $m = 5$, $\mu = 0$ and $H = 1/3$. At large scales, these PDFs match the standard Gaussian (in gray), while at small scales they tend to the velocity gradient PDF (in black). In (b), the velocity gradient PDF is shown for different values of the ensemble parameter m and compared to power-law fits with the fixed exponent $-m/H - 1$.

Another interesting connection one can draw is with more general multifractal models. In [62], for instance, a mixture of Gaussian fields with multifractal statistics is built. However, the

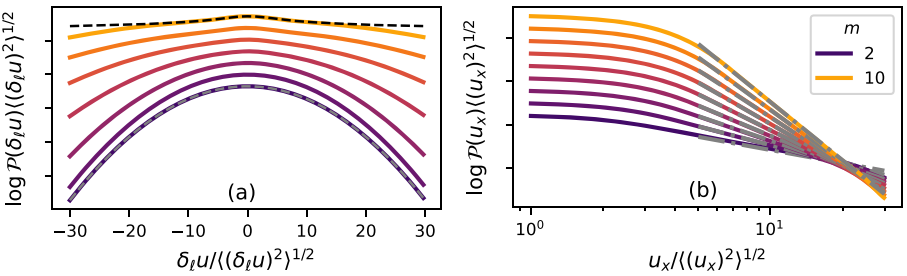

Fig. 11 Standardized PDFs of increments and gradients with nonsmooth subensembles. (a) shows increment PDFs (colors) compared to a Gaussian (gray) and the velocity gradient PDF (black). (b) shows the power-law decay in the tails of the velocity gradient PDFs for different values of m. In gray, power-law fits with a fixed exponent $-m/H - 1$, obtained in Eq. (56), are shown. PDFs have been arbitrarily shifted vertically for ease of visualization

subensembles are not exactly monofractal, due to the nonlinear transform that is performed. We highlight that our strategy uses monofractal subensembles instead, and allows us to deal with the singular distribution for the Hölder exponents in a bifractal model.

8 Discussions and Conclusions

This research has explored an ensemble of nearly-Gaussian characteristic functionals as a model for intermittent and skewed field statistics. This is a step towards a full statistical description of turbulent velocity fields compatible with the multifractal phenomenology. We obtain a one-dimensional field with Gaussian velocity statistics, together with bifractal increment and velocity gradient statistics.

As observed in [20], if the ensemble decomposition parameter is the typical scale s of the two-point correlation function, the resulting distribution shows intermittent behavior. With this choice, and an ensemble distribution which behaves asymptotically as $f_m(s) \sim s^{m-1}$ for small s, we have shown that the exponents for the increment and velocity gradient statistics are bifractal, namely

$$\langle(\delta_\ell u)^p\rangle \propto \ell^{\min(m,p)} \quad \text{and} \quad \langle(u_x)^p\rangle \propto \mathrm{Re}^{\max(0,p-m)}. \tag{57}$$

The velocity gradient scaling is furthermore compatible with the multifractal description of [11, 12], in which the velocity gradient exponents are derived from the increment exponents.

Skewness was added to this formulation with a functional equivalent to a Gram-Charlier A series, as an approximation to weakly non-Gaussian fields. The skewness term corresponds to the addition of a three-point correlation function with a typical scale s, the same as in the two-point correlation function.

Setting $m = 1$, the increment and gradient statistics agree with those of the stochastic Burgers velocity field. However, the velocity gradient PDF shows a different scaling, with a decay $|u_x|^{-m-1}$, while in the inviscid Burgers case the negative gradient tail is given by $|u_x|^{-7/2}$ [40, 41]. The source of this discrepancy is the symmetric decay of the positive and negative envelopes of the Airy function, used to add skewness.

The result we obtain for the PDFs, however, is similar to models with quenched disorder, see [50, Eq. 33]. Inspired by these models and by the multifractal scaling in Navier-Stokes, we have extended the construction to nonsmooth subensembles, where a Hölder exponent

$0 < H < 1$ is defined. This is done by choosing two and three-point functions similar to the Matérn covariance, therefore changing the scaling of the bifractal observables.

As further directions in the construction of the probability distribution of turbulent fields, we mention recent work on a Gaussian ensemble with multifractal scaling [62]. Furthermore, a functional description of skeweness without an approximation such as the Gram-Charlier A series is a challenge still open. Such a functional with skewed marginals would enable, for instance, the numerical sampling of skewed and bifractal velocity fields. Similarly to the symmetric case, one would sample a value of s from the PDF f_m, and use Gibbs sampling for the subensemble field: That is, sequentially sample values u_i, conditional on all previous $(u_j)_{j<i}$. The conditional distributions can be computed analytically or numerically, given the full characteristic functional. An issue with the current truncated characteristic functional in this sampling approach, though, are the negative excursions in the increment PDFs. Even though these excursions are small, they may lead to unexpected effects in the sampling algorithm.

Appendix A Proofs

A.1 A Helpful Result

In the following sections, we provide proofs of the scaling results in the main text. In the proofs we consider functions (say F) which represent a subensemble structure function (e.g. powers of S_2 in Eq. (24) or combinations of S_2 and S_3 in Eq. (39)) or the ensemble distribution f_m.

We focus on the asymptotic properties of these functions, namely a power-law behavior near the origin,

$$F(z) \underset{z\to 0^+}{\sim} cz^n, \; n > 0, \tag{A1}$$

and some well known behavior at large scales,

$$F(z) \underset{z\to\infty}{\sim} G(z). \tag{A2}$$

For even-order structure functions, G is a constant, while for odd-order ones it decays rapidly. The asymptotic notation is defined similarly to Eq. (17):

$$F(z) \underset{z\to L}{\sim} G(z) \;\text{ iff }\; \lim_{z\to L} \frac{F(z)}{G(z)} = 1. \tag{A3}$$

Furthermore, F is continuous, since it is built as a linear combination of continuous functions.

We use this information to replace the analysis of F by the analysis of a simpler, piecewise, function. For that we define an intermediate point z_0 (for instance, the solution to $cz_0^n = G(z_0)$), such that we can write

$$C_1 \left(z^n \mathbf{1}_{z\le z_0} + G(z)\mathbf{1}_{z>z_0}\right) < F(z) < C_2 \left(z^n \mathbf{1}_{z\le z_0} + G(z)\mathbf{1}_{z>z_0}\right), \tag{A4}$$

with real constants $C_2 > C_1$, and the indicator function represented by $\mathbf{1}$.

A.2 Proof of Eqs. (19) and (20)

Consider a function F as a smooth subensemble structure function of order n. With Eq. (A4), it can be bounded above and below by a constant times $(z^n \mathbf{1}_{z\le z_0} + M\mathbf{1}_{z>z_0})$, with M finite.

Using this bound, we will show there are parameters A, B which depend on the constants m, n, η, but not on the scale ℓ, such that, if $\ell, \eta, m > 0$, and $m \neq n$, then

$$\int_0^\eta \mathrm{d}s\, F(\ell/s)(s/\eta)^{m-1} \underset{\ell\to 0^+}{\sim} A_{m,n,\eta}(\ell/\eta)^m + B_{m,n,\eta}(\ell/\eta)^n. \tag{A5}$$

Furthermore, if $m = n$, there is an equivalent parameter C such that

$$\int_0^\eta \mathrm{d}s\, F(\ell/s)(s/\eta)^{m-1} \underset{\ell\to 0^+}{\sim} C_{m,\eta}(\ell/\eta)^m \log(\eta/\ell). \tag{A6}$$

Proof Using the bounds for F, we will show that

$$\lim_{\ell\to 0^+} \frac{\int_0^\eta \mathrm{d}s\, \left((\ell/s)^n \mathbf{1}_{\ell/s\le z_0} + M\mathbf{1}_{\ell/s>z_0}\right)(s/\eta)^{m-1}}{A_{m,n,\eta}(\ell/\eta)^m + B_{m,n,\eta}(\ell/\eta)^n} = \text{const.} \tag{A7}$$

With the substitution $z = \ell/s$, we obtain

$$\frac{\int_0^\eta \mathrm{d}s\, F(\ell/s)(s/\eta)^{m-1}}{A_{m,n,\eta}(\ell/\eta)^m + B_{m,n,\eta}(\ell/\eta)^n} = \lim_{\ell\to 0^+} \ell \frac{\int_{\ell/\eta}^\infty \frac{\mathrm{d}z}{z^2}\left(z^n \mathbf{1}_{z\le z_0} + M\mathbf{1}_{z>z_0}\right)(\ell/z\eta)^{m-1}}{A_{m,n,\eta}(\ell/\eta)^m + B_{m,n,\eta}(\ell/\eta)^n}, \tag{A8}$$

which is equal to

$$\lim_{\ell\to 0^+} \eta(\ell/\eta)^m \frac{\int_{\ell/\eta}^{z_0} \mathrm{d}z\, z^{n-m-1} + M\int_{z_0}^\infty \mathrm{d}z\, z^{-m-1}}{A_{m,n,\eta}(\ell/\eta)^m + B_{m,n,\eta}(\ell/\eta)^n}. \tag{A9}$$

The first integral reduces to

$$\lim_{\ell\to 0^+} \frac{\eta}{(m-n)}(\ell/\eta)^m \frac{(\ell/\eta)^{n-m} - z_0^{n-m}}{A_{m,n,\eta}(\ell/\eta)^m + B_{m,n,\eta}(\ell/\eta)^n} = \begin{cases} \frac{\eta}{B_{m,n,\eta}(m-n)}, & \text{if } m > n, \\ \frac{\eta z_0^{n-m}}{A_{m,n,\eta}(m-n)}, & \text{if } n > m. \end{cases} \tag{A10}$$

And the second integral to

$$\lim_{\ell\to 0^+} \eta M(\ell/\eta)^m \frac{\int_{z_0}^\infty \mathrm{d}z\, z^{-m-1}}{A_{m,n,\eta}(\ell/\eta)^m + B_{m,n,\eta}(\ell/\eta)^n} = \begin{cases} 0, & \text{if } m > n, \\ \frac{\eta M z_0^{-m}}{A_{m,n,\eta} m}, & \text{if } n > m, \end{cases} \tag{A11}$$

given that $m > 0$. The precise constants, as well as A, B, depend on the exact form of F, but the asymptotic behavior of the statement holds. This concludes the proof of Eq. (A5).

We can prove Eq. (A6) with the same strategy:

$$\begin{aligned} \frac{\int_0^\eta \mathrm{d}s\, F(\ell/s)(s/\eta)^{m-1}}{C_{m,\eta}(\ell/\eta)^m + \log(\eta/\ell)} &= \lim_{\ell\to 0^+} \frac{\int_0^\eta \mathrm{d}s\, \left((\ell/s)^m \mathbf{1}_{\ell/s\le z_0} + M\mathbf{1}_{\ell/s>z_0}\right)(s/\eta)^{m-1}}{C_{m,\eta}(\ell/\eta)^m \log(\eta/\ell)} \\ &= \frac{\eta}{C_{m,\eta}} \lim_{\ell\to 0^+} (\ell/\eta)^m \frac{\int_{\ell/\eta}^{z_0} \mathrm{d}z\, z^{-1} + \int_{z_0}^\infty \mathrm{d}z\, z^{-m-1}}{(\ell/\eta)^m \log(\eta/\ell)} \\ &= \frac{\eta}{C_{m,\eta}}(1+0). \end{aligned} \tag{A12}$$

□

Notice that, in Eqs. (A5) and (A6), we assumed the ensemble distribution to be the Beta distribution, with support $0 < s < \eta$. For a more general choice, one can use the bounds

$$\begin{aligned} D_1\left((s/\eta)^{m-1}\mathbf{1}_{s\le s_0} + f_\infty(s/\eta)\mathbf{1}_{z>z_0}\right) &\le f_m(s/\eta) \\ &\le D_2\left((s/\eta)^{m-1}\mathbf{1}_{s\le s_0} + f_\infty(s/\eta)\mathbf{1}_{z>z_0}\right), \end{aligned} \tag{A13}$$

with $0 < D_1 < D_2$ and where f_∞ may be the asymptotic form of f_m at large arguments. The proofs then follow in an equivalent manner, given that f_∞ decays sufficiently fast (faster than any polynomial, for instance).

It was also assumed for simplicity that F represents a smooth structure function of order n, however the proofs are also valid if one replaces $n \to nH$, where $H > 0$ is the Hölder parameter.

A.3 Proof of Eq. (29)

Let $\mathcal{C}$ and $\mathcal{S}$ be decaying and once differentiable functions, and define

$$C_2(y; s, \nu) = \mathcal{C}\left(\frac{y^2+\nu^2}{s^2}\right) \text{ and } C_3(x, y; s, \nu) = \left(\frac{x+y}{s}\right)\mathcal{S}\left(\frac{x^2+y^2+\nu^2}{s^2}\right). \quad \text{(A14)}$$

Then, the velocity-gradient functions G_2 and G_3 defined as in the main text (Eqs. (27) and (38)) are

$$G_2(s, \nu) = -2\mathcal{C}'(\nu^2/s^2)/s^2 \text{ and } G_3(s, \nu) = 4\mathcal{S}'(\nu^2/s^2)/s^3. \quad \text{(A15)}$$

The statistical moments of u_x and $|u_x|$ are built from these functions with Eqs. (41) and (43). Given that $\mathcal{C}$ and $\mathcal{S}$ decay sufficiently fast, the asymptotic behavior of the nth moment of either gradients or absolute-value gradients is $G(s, \nu) \sim s^{-n}\mathcal{G}(\nu^2/s^2)$, where $\mathcal{G}$ is a decaying function with $\mathcal{G}_0 = \mathcal{G}(0) \neq 0$.

We are going to show that, for some parameters A, B and C independent on ν, if $m \neq n$:

$$\lim_{\nu\to 0^+} \frac{\int_0^\eta \mathrm{d}s\, G(s, \nu)(s/\eta)^{m-1}}{A_{m,n,\eta}(\nu/\eta)^{m-n} + B_{m,n,\eta}} = 1, \quad \text{(A16)}$$

and if $m = n$,

$$\lim_{\nu\to 0^+} \frac{\int_0^\eta \mathrm{d}s\, G(s, \nu)(s/\eta)^{m-1}}{C_{m,\eta}\log(\eta/\nu)} = 1. \quad \text{(A17)}$$

Proof First, let us comment on $\mathcal{G}$. The subensemble gradient moments are

$$\langle (u_x)^p \rangle_s = B_p(0, G_2(s, \nu), G_3(s, \nu), 0, \ldots, 0), \quad \text{(A18)}$$

and the respective absolute gradient moments are

$$\langle |u_x|^p \rangle_s = G_2(s, \nu)^{p/2}\, {}_1F_1\left(-\frac{p}{2}, \frac{1}{2}; -\frac{1}{2}\left(\frac{G_3^{2/3}(s, \nu)}{G_2(s, \nu)}\right)\right), \quad \text{(A19)}$$

with ${}_1F_1$ the Kummer confluent hypergeometric function. These functions are proportional to s^{-p} and converge to a fixed value ($\mathcal{G}_0$) as $\nu \to 0$.

With Eq. (A4), we write

$$C_1\left(s^{-n}\mathcal{G}_0\mathbf{1}_{\nu/s\le z_0} + M\mathbf{1}_{\nu/s>z_0}\right) < G(s, \nu) < C_2\left(s^{-n}\mathcal{G}_0\mathbf{1}_{\nu/s\le z_0} + M\mathbf{1}_{\nu/s>z_0}\right). \quad \text{(A20)}$$

This is a very crude approximation, since $\mathcal{G}$ is a decaying function. With the substitution $z = \nu/s$

$$\lim_{\nu\to 0^+} \nu \frac{\int_{\nu/\eta}^{z_0} \frac{\mathrm{d}z}{z^2}(\nu/z)^{-n}\mathcal{G}_0(\nu/\eta z)^{m-1} + M\int_{z_0}^{+\infty}\frac{\mathrm{d}z}{z^2}(\nu/\eta z)^{m-1}}{A_{m,n,\eta}(\nu/\eta)^{m-n} + B_{m,n,\eta}} = 1. \quad \text{(A21)}$$

The first integral has two contributions, one proportional to ν^{m-n} and the other to ν^0. The second one contains a ν^m term. Since $m > 0$, the dominant contribution is either $m - n$, when $n > m$, or 0, otherwise. Furthermore, both integrals converge.

In the case $m = n$, the numerator after the substitution is

$$\lim_{\nu\to 0^+} \eta^{-m+1} \frac{\int_{\nu/\eta}^{z_0} \frac{\mathrm{d}z}{z}\, \mathcal{G}_0 + \nu^m M \int_{z_0}^{+\infty} \frac{\mathrm{d}z}{z^2} z^{m-1}}{C_{m,\eta} \log(\eta/\nu)} = 1. \tag{A22}$$

Once again, the first integral is proportional to $\log(\eta/\nu)$, while the second term is regular and proportional to ν^m. □

A.4 Proof of $\mathcal{P}_{u_x}(\xi) \sim \xi^{-m-1}$ (Eq. 28)

In order to compute the large fluctuation behavior of the velocity gradient PDF,

$$\mathcal{P}_{u_x}(\xi) = \int_0^\infty \mathrm{d}s\; f_m(s;\eta)\, \frac{s}{\sqrt{2\pi}\sigma} e^{-\frac{1}{2}(s\xi/\sigma)^2}, \tag{A23}$$

define $z = s/\eta$ and use Eq. (A4) to write

$$C_1 \left(z^{m-1}\mathbf{1}_{z\le z_0} + \mathbf{1}_{z>z_0}\right) \le f_m(\eta z;\eta) \le C_2 \left(z^{m-1}\mathbf{1}_{z\le z_0} + \mathbf{1}_{z>z_0}\right). \tag{A24}$$

This is a quite radical modification of f_m since it cannot be normalized, but it simplifies the computations to follow. Modifying the $z > z_0$ part to include a decaying function does not change the proof. We will compute an upper and a lower bound for

$$\mathcal{P}_{u_x}(\xi) = \eta \int_0^\infty \mathrm{d}z\; f_m(\eta z;\eta)\, \frac{\eta z}{\sqrt{2\pi}\sigma} e^{-\frac{1}{2}(\eta z\xi/\sigma)^2}. \tag{A25}$$

With the change of variables $\rho = \eta z\xi/\sigma$, the $z \le z_0$ term in the above integral is bounded by

$$\xi^{-m-1} \times C_2 \frac{(\sigma/\eta)^m}{\sqrt{2\pi}} \int_0^{\eta z_0 \xi/\sigma} \mathrm{d}\rho\; \rho^m e^{-\frac{1}{2}\rho^2}. \tag{A26}$$

In the limit $\xi \to \infty$, the integral is finite for any $m > -1$. The $z > z_0$ integral also converges, and is bounded above by

$$\xi^{-1} \times C_2 \frac{\eta}{\sqrt{2\pi}} \int_{\eta z_0 \xi/\sigma}^\infty \mathrm{d}\rho\; \rho\, e^{-\frac{1}{2}\rho^2}. \tag{A27}$$

For the lower bound, simply replace C_2 with C_1. Therefore, in the limit $\xi \to \infty$, with $m > 0$, Eq. (A26) is the main contribution to the asymptotic behavior of $\mathcal{P}_{u_x}(\xi)$.

A.5 Proof of Eq. (44a) and the limit $\mathcal{P}_{u_x}(\xi) \sim \xi^{-m-1}$

Consider $\mathcal{C}$ and $\mathcal{S}$ as defined in Eq. (A14). The subensemble characteristic function of the skewed velocity gradient is

$$\Phi_{u_x}(\alpha; s) = \exp\left\{-\frac{\alpha^2\sigma^2|\mathcal{C}'(0)|}{s^2} - \frac{2i\alpha^3\mu^3\mathcal{S}'(0)}{3s^3}\right\}, \tag{A28}$$

with $\mathcal{C}$ and $\mathcal{S}$ as defined in Eq. (A14). Using the Airy formula, this is rewritten as

$$\Phi_{u_x}(\alpha; s) = \int_{\mathbb{R}} \mathrm{d}y\, \mathrm{Ai}(y) \exp\left\{\frac{i\alpha\mu y\sqrt[3]{2\mathcal{S}'(0)}}{s} - \frac{\alpha^2\sigma^2|\mathcal{C}'(0)|}{s^2}\right\}, \tag{A29}$$

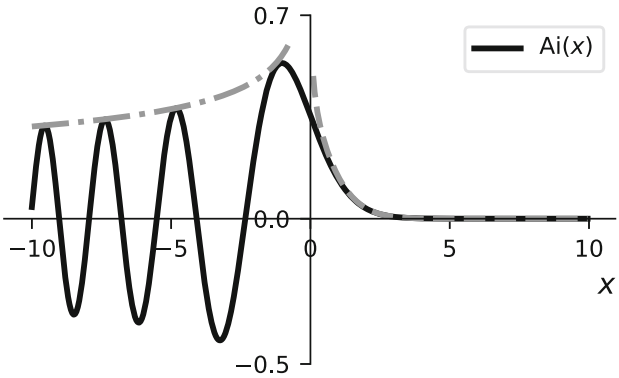

Fig. 12 A plot of the Airy function (black) together with its right asymptotic limit (gray dashed) and its left upper envelope (gray dash-dotted)

whose corresponding PDF is

$$\mathcal{P}_{u_x}(\xi;s) = \int_{\mathbb{R}} \mathrm{d}y\, \mathrm{Ai}(y) \frac{s}{2\sqrt{\pi|\mathcal{C}'(0)|}\sigma} \exp\left\{-\frac{s^2}{4|\mathcal{C}'(0)|\sigma^2}\left(\xi - \sqrt[3]{2\mathcal{S}'(0)}\mu y/s\right)^2\right\}. \tag{A30}$$

This expression can be integrated analytically [47, Eq. 3.10],

$$\begin{aligned}\mathcal{P}_{u_x}(\xi;s) = {} & \frac{s}{\sqrt[3]{2\mathcal{S}'(0)}\mu} \exp\left\{\frac{3|\mathcal{C}'(0)|\mathcal{S}'(0)\mu^3\sigma^2 s\xi + |\mathcal{C}'(0)|^3\sigma^6}{6\mathcal{S}'^2(0)\mu^6}\right\} \\ & \times \mathrm{Ai}\left(\frac{2\mathcal{S}'(0)\mu^3 s\xi + \mathcal{C}'^2(0)\sigma^4}{(2\mathcal{S}'(0))^{4/3}\mu^4}\right).\end{aligned} \tag{A31}$$

To obtain an asymptotic behavior, we will use the following expressions [63, Eqs. 11.1.07 and 11.1.08]:

$$\mathrm{Ai}(x) \underset{x\to\infty}{\sim} \frac{e^{-\frac{2}{3}x^{3/2}}}{2\sqrt{\pi}x^{1/4}}, \text{ and} \tag{A32a}$$

$$\mathrm{envAi}(x) \underset{x\to-\infty}{\sim} \frac{1}{\sqrt{\pi}|x|^{1/4}}, \text{ for the upper envelope of the Airy function.} \tag{A32b}$$

The Airy function and its asymptotic limits are illustrated in Fig. 12.

Let us consider $\mu > 0$, corresponding to negative velocity gradient skewness, since $\mathcal{S}'(0) < 0$. In this case, the negative oscillations in the Airy function belong to the right side of the gradient PDF, Eq. (A31), whose asymptotic limits are

$$\begin{aligned}\mathcal{P}_{u_x}(\xi;s) \underset{\xi\to-\infty}{\sim} {} & \frac{s}{\sqrt[3]{2\mathcal{S}'(0)}\mu} \frac{(2|\mathcal{S}'(0)|)^{1/12}}{\sqrt{\pi}} |\mu/s\xi|^{1/4} \\ & \times \exp\left\{-\frac{\sqrt{2}|s\xi/\mu|^{3/2}}{3\sqrt{|\mathcal{S}'(0)|}} + O(\xi)\right\},\end{aligned} \tag{A33a}$$

$$\mathrm{env}\mathcal{P}_{u_x}(\xi;s) \underset{\xi\to\infty}{\sim} \frac{s}{\sqrt[3]{2\mathcal{S}'(0)}\mu} \exp\left\{\frac{|\mathcal{C}'(0)|\sigma^2 s\xi}{2\mathcal{S}'(0)\mu^3}\right\} \frac{(2|\mathcal{S}'(0)|)^{1/12}}{\sqrt{\pi}} |\mu/s\xi|^{1/4}. \tag{A33b}$$

Integrating against the ensemble distribution f_m (which can also be written in terms of the bounds in Eq. (A4)), we obtain expressions of the type

$$\mathcal{P}_{u_x}(\xi; s) \underset{\xi\to-\infty}{\sim} \int_0^{z_0} \mathrm{d}z\, z^{m-1} \times z \frac{e^{-(z|\xi|)^{3/2}}}{|z\xi|^{1/4}} = \xi^{-m-1} \int_0^{u_0} \mathrm{d}u\, u^{m-1/4} e^{-u^{3/2}}, \tag{A34}$$

for the negative tail and

$$\mathrm{env}\mathcal{P}_{u_x}(\xi; s) \underset{\xi\to\infty}{\sim} \int_0^{z_0} \mathrm{d}z\, z^{m-1} \times z \frac{e^{-|z\xi|}}{|z\xi|^{1/4}} = \xi^{-m-1} \int_0^{u_0} \mathrm{d}u\, u^{m-1/4} e^{-u}, \tag{A35}$$

for the envelope of the positive tail. To make these equations more transparent, all constants have been suppressed. In particular, since $\mathcal{S}$ is assumed to be a decaying function, the replacement $\mathcal{S}'(0) \to -1$ was done. Both integrals on the right-hand side are finite, and the power-law tail behavior is highlighted.

Acknowledgements We thank M. Bernard for bringing [50] to our attention.

Funding Open Access funding enabled and organized by Projekt DEAL. This project has received funding from the European Research Council (ERC) under the European Union's Horizon 2020 research and innovation programme (Grant agreement No. 101001081).

Data Availability Computer programs written for this study are available upon request.

Declarations

Conflicts of interest The authors report no conflict of interest.

Open Access This article is licensed under a Creative Commons Attribution 4.0 International License, which permits use, sharing, adaptation, distribution and reproduction in any medium or format, as long as you give appropriate credit to the original author(s) and the source, provide a link to the Creative Commons licence, and indicate if changes were made. The images or other third party material in this article are included in the article's Creative Commons licence, unless indicated otherwise in a credit line to the material. If material is not included in the article's Creative Commons licence and your intended use is not permitted by statutory regulation or exceeds the permitted use, you will need to obtain permission directly from the copyright holder. To view a copy of this licence, visit http://creativecommons.org/licenses/by/4.0/.

References

1. Taylor, G.I.: Statistical theory of turbulence. P. Roy. Soc. A - Math. Phy. **151**(873), 421–444 (1935)
2. Sreenivasan, K.R., Antonia, R.A.: The phenomenology of small-scale turbulence. Annu. Rev. Fluid Mech. **29**(1), 435–472 (1997)
3. Ishihara, T., Gotoh, T., Kaneda, Y.: Study of high-Reynolds number isotropic turbulence by direct numerical simulation. Annu. Rev. Fluid Mech. **41**(1), 165–180 (2009)
4. Buaria, D., Sreenivasan, K.R.: Saturation and multifractality of Lagrangian and Eulerian scaling exponents in three-dimensional turbulence. Phys. Rev. Lett. **131**(20), 204001 (2023)
5. Lashermes, B., Roux, S.G., Abry, P., Jaffard, S.: Comprehensive multifractal analysis of turbulent velocity using the wavelet leaders. Eur. Phys. J. B **61**, 201–215 (2008)
6. Frisch, U.: Turbulence: the Legacy of A N. Kolmogorov. Cambridge University Press, Cambridge (1995)
7. Beck, C.: Statistics of three-dimensional Lagrangian turbulence. Phys. Rev. Lett. **98**(6), 064502 (2007)
8. Bentkamp, L., Lalescu, C.C., Wilczek, M.: Persistent accelerations disentangle Lagrangian turbulence. Nat. Comms. **10**(1), 3550 (2019)
9. Chevillard, L., Castaing, B., Arneodo, A., Lévêque, E., Pinton, J.-F., Roux, S.G.: A phenomenological theory of Eulerian and Lagrangian velocity fluctuations in turbulent flows. C R Phys. **13**(9–10), 899–928 (2012)

10. Sosa-Correa, W., Pereira, R.M., Macêdo, A.M.S., Raposo, E.P., Salazar, D.S.P., Vasconcelos, G.L.: Emergence of skewed non-Gaussian distributions of velocity increments in isotropic turbulence. Phys. Rev. Fluids **4**(6), 064602 (2019)
11. Nelkin, M.: Multifractal scaling of velocity derivatives in turbulence. Phys. Rev. A **42**(12), 7226 (1990)
12. Chakraborty, S., Frisch, U., Pauls, W., Ray, S.S.: Nelkin scaling for the Burgers equation and the role of high-precision calculations. Phys. Rev. E **85**(1), 015301 (2012)
13. Benzi, R., Biferale, L., Fisher, R., Lamb, D.Q., Toschi, F.: Inertial range Eulerian and Lagrangian statistics from numerical simulations of isotropic turbulence. J. Fluid Mech. **653**, 221–244 (2010)
14. Benzi, R., Biferale, L., Toschi, F.: Multiscale velocity correlations in turbulence. Phys. Rev. Lett. **80**(15), 3244 (1998)
15. Friedrich, J., Margazoglou, G., Biferale, L., Grauer, R.: Multiscale velocity correlations in turbulence and Burgers turbulence: Fusion rules, Markov processes in scale, and multifractal predictions. Phys. Rev. E **98**(2), 023104 (2018)
16. Titterington, D.M., Smith, A.F.M., Makov, U.E.: Statistical Analysis of Finite Mixture Distributions. John Wiley & Sons, Chichester (1985)
17. Reynolds, D.A., Rose, R.C.: Robust text-independent speaker identification using Gaussian mixture speaker models. IEEE Trans. Audio Speech Lang. Process. **3**(1), 72–83 (1995)
18. Ruan, L., Yuan, M., Zou, H.: Regularized parameter estimation in high-dimensional Gaussian mixture models. Neural Comput. **23**(6), 1605–1622 (2011)
19. Zhang, L., Risser, M.D., Molter, E.M., Wehner, M.F., O'Brien, T.A.: Accounting for the spatial structure of weather systems in detected changes in precipitation extremes. Weather Clim. Extrem. **38**, 100499 (2022)
20. Wilczek, M.: Non-Gaussianity and intermittency in an ensemble of Gaussian fields. N. J. Phys. **18**, 125009 (2016)
21. Hengster, Y.: Curvature statistics of turbulence, School of Mathematics, University of Edinburgh (2025). (PhD thesis)
22. Matsubara, T.: Statistics of smoothed cosmic fields in perturbation theory. I. formulation and useful formulae in second-order perturbation theory. Astrophys. J. 584(1), 1 (2003)
23. Longuet-Higgins, M.S.: The effect of non-linearities on statistical distributions in the theory of sea waves. J. Fluid Mech. **17**(3), 459–480 (1963)
24. Fuhrman, D.R., Klahn, M., Zhai, Y.: A new probability density function for the surface elevation in irregular seas. J. Fluid Mech. **970**, 38 (2023)
25. Aurell, E., Frisch, U., Lutsko, J., Vergassola, M.: On the multifractal properties of the energy dissipation derived from turbulence data. J. Fluid Mech. **238**, 467–486 (1992)
26. Boritchev, A., Kuksin, S.: One-dimensional Turbulence and the Stochastic Burgers Equation, vol. 255. American Mathematical Soc, Providence, RI (2021)
27. De, S., Mitra, D., Pandit, R.: Uncovering the multifractality of Lagrangian pair dispersion in shock-dominated turbulence. Phys. Rev. Res. **6**(2), 022032 (2024)
28. Iyer, K.P., Sreenivasan, K.R., Yeung, P.K.: Circulation in high Reynolds number isotropic turbulence is a bifractal. Phys. Rev. X **9**(4), 041006 (2019)
29. Müller, N.P., Polanco, J.I., Krstulovic, G.: Intermittency of velocity circulation in quantum turbulence. Phys. Rev. X **11**(1), 011053 (2021)
30. Soriano, J., Ortín, J., Hernández-Machado, A.: Anomalous roughening in experiments of interfaces in Hele-Shaw flows with strong quenched disorder. Phys. Rev. E **67**(5), 056308 (2003)
31. Benton, E.R.: Solutions illustrating the decay of dissipation layers in Burgers' nonlinear diffusion equation. Phys. Fluids **10**(10), 2113–2119 (1967)
32. Eyink, G.L.: Turbulence Theory: course notes. https://www.ams.jhu.edu/%7Eeyink/Turbulence/notes.html. Accessed: 2025-10-24 (2007-2008)
33. E, W., Vanden-Eijnden, E.: Statistical theory for the stochastic Burgers equation in the inviscid limit. Commun. Pure Appl. Math. 53(7), 852–901 (2000)
34. Gurarie, V., Migdal, A.: Instantons in the Burgers equation. Phys. Rev. E **54**(5), 4908 (1996)
35. Balkovsky, E., Falkovich, G., Kolokolov, I., Lebedev, V.: Intermittency of Burgers' turbulence. Phys. Rev. Lett. **78**(8), 1452 (1997)
36. Cardy, J., Falkovich, G., Gawędzki, K.: Non-equilibrium Statistical Mechanics and Turbulence. London Mathematical Society Lecture Note Series, vol.355. Cambridge University Press, Cambridge (2008)
37. Chernykh, A.I., Stepanov, M.G.: Large negative velocity gradients in Burgers turbulence. Phys. Rev. E **64**, 026306 (2001)
38. Grafke, T., Grauer, R., Schäfer, T., Vanden-Eijnden, E.: Relevance of instantons in Burgers turbulence. Europhys. Lett. **109**, 34003 (2015)

39. Apolinário, G.B., Moriconi, L., Pereira, R.M.: Onset of intermittency in stochastic Burgers hydrodynamics. Phys. Rev. E **99**(3), 033104 (2019)
40. Khanin, E.W., Mazel, K., Sinai, A., Y.: Probability distribution functions for the random forced Burgers equation. Phys. Rev. Lett. **78**(10), 1904 (1997)
41. Bec, J.: Universality of velocity gradients in forced Burgers turbulence. Phys. Rev. Lett. **87**(10), 104501 (2001)
42. Lukacs, E.: Characteristic Functions. Griffin, London (1970)
43. Risken, H.: The Fokker-Planck Equation. Springer, Heidelberg (1996)
44. Comtet, L.: Advanced Combinatorics: The Art of Finite and Infinite Expansions. Springer, Dordrecht, Holland (1974)
45. Calabrese, P., Le Doussal, P., Rosso, A.: Free-energy distribution of the directed polymer at high temperature. Europhys. Lett. **90**(2), 20002 (2010)
46. Dotsenko, V., Klumov, B.: Bethe ansatz solution for one-dimensional directed polymers in random media. J. Stat. Mech. **2010**(03), 03022 (2010)
47. Katori, M., Tanemura, H.: Zeros of Airy function and relaxation process. J. Stat. Phys. **136**(6), 1177–1204 (2009)
48. Gotoh, T., Kraichnan, R.H.: Steady-state Burgers turbulence with large-scale forcing. Phys. Fluids **10**(11), 2859–2866 (1998)
49. Gärtner, J., Den Hollander, F., Maillard, G.: Quenched Lyapunov exponent for the parabolic Anderson model in a dynamic random environment. In: Probability in Complex Physical Systems. In Honour of Erwin Bolthausen and Jürgen Gärtner, pp. 159–193. Springer, Berlin, Heidelberg (2011)
50. Bernard, M., Le Doussal, P., Rosso, A., Texier, C.: Anomalous scaling of heterogeneous elastic lines: A picture from sample-to-sample fluctuations. Phys. Rev. E **110**(1), 014104 (2024)
51. Bentkamp, L., & Wilczek, M. (2026). Statistical field theory for a passive vector model with spatially linear advection. Physical Review Fluids, 11(7), 074606
52. Lübke, J., Friedrich, J., Grauer, R.: Stochastic interpolation of sparsely sampled time series by a superstatistical random process and its synthesis in Fourier and wavelet space. J. Phys.: Complexity **4**(1), 015005 (2023)
53. Mukherjee, S., Murugan, S.D., Mukherjee, R., Ray, S.S.: Turbulent flows are not uniformly multifractal. Phys. Rev. Lett. **132**(18), 184002 (2024)
54. The mpmath development team: mpmath: a Python Library for Arbitrary-precision Floating-point Arithmetic (version 1.3.0). (2023). http://mpmath.org/
55. Kolmogorov, A.N.: The local structure of turbulence in incompressible viscous fluid for very large reynolds numbers. Cr. Acad. Sci. URSS **30**, 301–305 (1941)
56. Wolf, D.E., Villain, J.: Growth with surface diffusion. Europhys. Lett. **13**(5), 389 (1990)
57. Sarma, S.D., Tamborenea, P.: A new universality class for kinetic growth: One-dimensional molecular-beam epitaxy. Phys. Rev. Lett. **66**(3), 325 (1991)
58. Williams, C.K.I., Rasmussen, C.E.: Gaussian Processes for Machine Learning. MIT press, Cambridge, MA (2006)
59. Stein, M.L.: Interpolation of Spatial Data: Some Theory for Kriging. Springer, New York, NY (2012)
60. Apolinário, G.B., Chevillard, L., Mourrat, J.-C.: Dynamical fractional and multifractal fields. J. Stat. Phys. **186**(1), 15 (2022)
61. Beck, G., Bréhier, C.-E., Chevillard, L., Grande, R., Ruffenach, W.: Numerical simulations of a stochastic dynamics leading to cascades and loss of regularity: Applications to fluid turbulence and generation of fractional Gaussian fields. Phys. Rev. Res. **6**(3), 033048 (2024)
62. Warnecke, M., Bentkamp, L., Apolinário, G. B., Wilczek, M., & Johnson, P. (2026). An ensemble of Gaussian fields with multifractal statistics for turbulence. Journal of Fluid Mechanics, 1035, A23
63. Olver, F.W.J.: Asymptotics and Special Functions. Academic Press, New York (1974)

Publisher's Note Springer Nature remains neutral with regard to jurisdictional claims in published maps and institutional affiliations.